Characterization of the arc in crossflow using a two-temperature nonequilibrium plasma flow model

V G Bhigamudre[1] **and J P Trelles**[1]

[1]Department of Mechanical Engineering, University of Massachusetts Lowell, 197 Riverside St., Lowell, MA 01854, USA

E-mail: Juan_Trelles@uml.edu

Abstract. Diverse industrial applications such as circuit breakers and wire arc spraying involve the interaction between an electric arc and a stream of gas impinging perpendicular to it, a configuration commonly referred to as the arc in crossflow. The arc in crossflow is simulated using a three-dimensional time-dependent two-temperature (heavy-species and electrons) plasma flow model to better capture plasma-gas interactions and deviations from Local Thermodynamic Equilibrium (LTE). The coupled fluid-electromagnetic flow model is solved in a monolithic manner using Variational Multiscale Finite Element Method. Simulation results are validated with experimental findings and contrasted against results obtained with a LTE model. Results from the two-temperature model corroborate experimental observations while providing quantification of the deviation between heavy-species and electron temperatures. The model is used to characterize the arc in crossflow as a function of the Reynolds and Enthalpy dimensionless numbers, which encapsulate the inter-dependence among the main parameters total current, inflow velocity, and inter-electrode spacing. The characterization revealed the behavior of arc shape, voltage drop, arc power, the degree of nonequilibrium, as well as the characteristic plasma front thickness, with varying controlling parameters.

Keywords: non-LTE, electric arc, plasma-gas interaction, atmospheric pressure nonequilibrium plasma

1. Introduction

1.1. *Motivation*

Arc discharge plasmas are extensively employed in diverse industrial applications such as spraying, welding, cutting, metallurgy, chemical and particle synthesis, resource recovery, etc. Among these, wire arc spraying and low-voltage circuit breakers are distinct applications that involve the interaction of an electric arc with a stream of working gas flow striking perpendicularly to it. Such a configuration is commonly referred to as the arc in crossflow. Greater understanding of the arc in

crossflow can provide fundamental understanding of plasma – gas flow interactions and aid in equipment design and industrial process optimization [1].

Wire arc spraying is a materials deposition technique used in applications such as corrosion and oxidation prevention, abrasion resistance, aircraft components, and medical implants that provides high material and energy efficiencies with lower capital and operating costs [2]. Low-voltage circuit breakers are one of the most widely used electrical safety components in battery systems, data centers, portable power devices, industrial machinery, switch gears, power breakers, etc. Figure 1 shows schematics of the wire arc spraying process and a low-voltage circuit breaker. The wire arc spraying system consists of metallic wires fed continuously to act as cathode and anode, which are subjected to a potential difference in the order of several kilovolts, leading to arc formation. The arc elongates downstream from the electrodes due to the action of impinging gas flow. The formed plasma melts the cathode and anode wires, and the gas flow drags the molten metal particles directing them to be deposited onto a substrate. In low-voltage circuit breakers, electrodes are in contact when the system is in the rest position. The system activates in the event of a high voltage leak in the electrical circuit, which in turn initiates a mechanism that separates the electrodes. The movement of electrodes leads to electric breakdown through the gap and the formation of an arc. The formed arc must be extinguished, which is typically attained by quenching using a metallic splitter and cold-gas flow. Wire arc spraying requires high plasma temperature (in the order of several kK) and high pressure (in the order of a few atm) to achieve better deposition of molten metal particles on the substrate [3]. In contrast, low-voltage circuit breakers require rapid plasma quenching to avoid thermal damages in the system. Thus, despite both applications possess markedly contrasting objectives and operational characteristics, they both are based on a similar plasma flow configuration, i.e., an arc in crossflow.

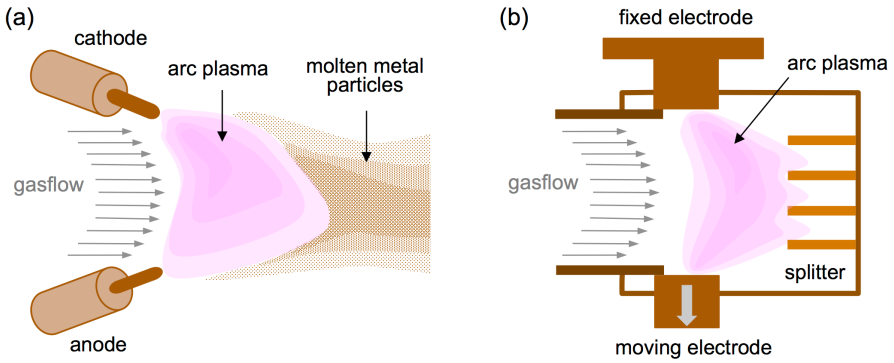

Figure 1. Schematics of industrial applications based on the arc in crossflow configuration: (a) wire arc spraying and (b) low-voltage circuit breakers.

Wire arc spraying and low-voltage circuit breakers have been extensively studied by diverse computational models with different degrees of fidelity. Bolot *et al* [2] developed a three-dimensional compressible flow model of wire arc spraying with a detailed description of the spatial domain that

captured gas-particle interactions but neglected electromagnetic effects, which are crucial to depict the dynamics of the arc. Circuit breakers [4-7] have been analyzed through models that rely on the Local Thermodynamic Equilibrium (LTE) assumption, i.e., the heavy-species (molecules, atoms, ions) are considered to be in thermodynamic equilibrium with the free electrons. The LTE assumption is typically valid within the arc plasma core, but can be inadequate for describing systems where the plasma interacts strongly with its surroundings, such as arc – electrode interfaces and arc – gas flow interactions. Therefore, models that overcome the LTE assumption by explicitly describing the inter-dependent dynamics of electron and heavy-species energies are prone to provide greater fidelity descriptions.

1.2. *The arc in crossflow*

A schematic of a canonical arc in crossflow system is shown in figure 2. The anode and the cathode are separated with inter-electrode spacing H and are confined within solid walls. A plasma arc is formed between the electrodes due to the imposition of a total amount of electric current I_{tot} from a power supply (not shown). The arc is subjected to a perpendicularly striking stream of processing gas flow with mean axial velocity U_i at the inlet. The gas flow causes convective cooling and drag on the arc. The net effect is characterized by the bending of the arc plasma column and the formation of an afterglow in the downstream region. The electrode attachment regions are constricted at the cathode and relatively diffuse at the anode. The plasma characteristics are mainly determined by the working gas properties, the inter-electrode spacing, the inlet velocity, and the imposed electrical current.

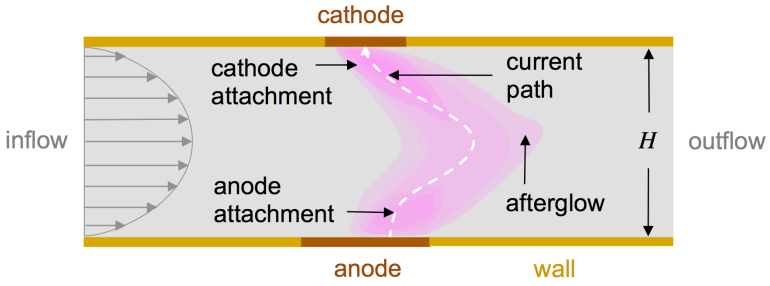

Figure 2. Schematics of a canonical arc in crossflow system.

The canonical arc in crossflow configuration has been studied by experimental, theoretical, and computational approaches. Benenson *et al* [8] have experimentally determined the radial temperature profile for various imposed currents using an integrated line emissions method and analyzed plasma arc profiles for varying current and gas-flow rates [9]. Maecker *et al* [10] developed an analytical model to define the arc formation and the arc bending using a simplified mathematical formulation. Kelkar *et al* [1] investigated the physics of the arc in crossflow using a three-dimensional (3D) LTE plasma model neglecting the effect of self-induced electromagnetic forces on the plasma. Lincun *et al* [11] conducted a parametric study of the arc in crossflow to examine the effects of axial velocity,

electrode spacing and imposed current using a 3D LTE model that included the effects of electromagnetic forces.

All previous computational investigations of the arc in crossflow have relied on models based on the LTE assumption, and therefore on the use of a single temperature to characterize the energy of the heavy-species and electrons. A two-temperature, non-LTE (NLTE) model, which explicitly describes the interdependency of the dynamics of the energy carried by heavy-species and by electrons, can provide novel fundamental insight of the characteristics of the arc in crossflow, particularly of the extent of thermal nonequilibrium and its potential effect on the arc dynamics.

1.3. *Scope and outline*

The article presents the characterization of the canonical argon arc in crossflow via three-dimensional time-dependent computational simulations. The physical-mathematical model, based on a chemical equilibrium and thermal nonequilibrium (NLTE) description of the flow, is described in Section 2. Section 3 presents the numerical formulation of the model and the solution approach. Section 4 presents the simulation setup, including the domain and imposed conditions. Representative simulation results, validation with experimental results, and comparison with LTE results are shown in Section 5. Section 6 discusses the computational characterization of the arc in crossflow, including controlling parameters and phenomenological properties. Conclusions are presented in Section 7.

2. Mathematical model

2.1. Assumptions

The plasma is considered as a compressible, reactive, electromagnetic fluid in chemical equilibrium and thermal nonequilibrium (NLTE); the plasma is assumed optically thin, quasi-neutral, and non-magnetized; ion diffusion and Hall currents are neglected; charge transport is dominated by the electric field distribution and electron diffusion; and electrode sheaths are neglected.

The optically thin assumption is used to make the computation tractable (i.e., instead of solving the non-gray Radiative Transfer Equation [12]). This approximation is expected to overestimate energy lost by radiation, but not to have a major effect on the resulting arc configuration [13]. Similarly, the neglect of sheaths is expected to mainly affect the predicted voltage drop across the arc and the energy transfer to the electrodes, but to have a minor effect on the overall arc and in the arc-gas interaction, which are the main focus of the study.

2.2. Model equations

The plasma flow model, based on the assumptions above, is constituted by the equations of conservation of: total mass, mass-average momentum, thermal energy of heavy-species, thermal

energy of electrons, electric charge, and the magnetic induction equation. These equations form a single set of transient-advective-diffusive-reactive (TADR) transport equations listed in table 1.

Table 1. Set of fluid-electromagnetic evolution equations for the two-temperature NLTE plasma flow model. For each equation: Transient + Advective – Diffusive − Reactive = 0.

Equation	Transient	Advective	Diffusive	Reactive
Mass conservation	$\partial_t \rho$	$\mathbf{u}\cdot\nabla\rho + \rho\nabla\cdot\mathbf{u}$	0	0
Momentum conservation	$\rho\partial_t \mathbf{u}$	$\rho\mathbf{u}\cdot\nabla\mathbf{u} + \nabla p$	$\nabla\cdot\mu(\nabla\mathbf{u} + \nabla\mathbf{u}^{\mathsf{T}}) - \nabla\cdot(\frac{2}{3}\mu(\nabla\cdot\mathbf{u})\boldsymbol{\delta})$	$\mathbf{J}_q \times \mathbf{B}$
Thermal energy heavy-species	$\rho\partial_t h_h$	$\rho\mathbf{u}\cdot\nabla h_h$	$\nabla\cdot(\kappa_{hr}\nabla T_h)$	$D_t p_h + K_{eh}(T_e - T_h) - \boldsymbol{\tau} : \nabla\mathbf{u}$
Thermal energy electrons	$\rho\partial_t h_e$	$\rho\mathbf{u}\cdot\nabla h_e$	$\nabla\cdot(\kappa_e\nabla T_e)$	$D_t p_e - K_{eh}(T_e - T_h) - 4\pi\varepsilon_r + \mathbf{J}_q\cdot(\mathbf{E} + \mathbf{u}\times\mathbf{B}) + \frac{5k_B}{2e}\mathbf{J}_q\cdot\nabla T_e$
Charge conservation	0	0	$\nabla\cdot(\sigma\nabla\phi_p) - \nabla\cdot(\sigma\mathbf{u}\times(\nabla\times\mathbf{A}))$	0
Magnetic induction	$\mu_0\sigma\partial_t\mathbf{A}$	$\mu_0\sigma\nabla\phi_p - \mu_0\sigma\mathbf{u}\times(\nabla\times\mathbf{A})$	$\nabla^2\mathbf{A}$	$\mathbf{0}$

In table 1, $\partial_t = \partial/\partial t$ represents the partial derivative with respect to time, ∇ and $\nabla\cdot$ represent the gradient and divergence operators, respectively; ρ is mass density, p pressure, $\mathbf{u}$ mass-averaged velocity, μ dynamic viscosity, $^{\mathsf{T}}$ the transpose operator, and $\boldsymbol{\delta}$ the Kronecker delta tensor; $\mathbf{J}_q$ x $\mathbf{B}$ represents the Lorentz force, where $\mathbf{J}_q$ is the electric current density and $\mathbf{B}$ is the self-induced magnetic field; $\mathbf{J}_q$ is calculated using the generalized Ohm's law: $\mathbf{J}_q = \sigma(\mathbf{E}_p + \mathbf{u}\times\mathbf{B})$, where $\mathbf{E}_p \approx \mathbf{E} + (\nabla p_e / e n_e)$ is the effective electric field, $\mathbf{E}$ is the real electric field, p_e electron pressure, n_e electron number density, k_B Boltzmann constant, and e the elementary electric charge; h_h and h_e are enthalpies of heavy-species and electrons, respectively; κ_{hr} is the translational-reactive thermal conductivity of heavy-species, κ_e is the translational thermal conductivity of electrons; $D_t p$ represents pressure work, where $D_t \equiv \partial_t + \mathbf{u}\cdot\nabla$ is the total derivative; K_{eh} is the energy exchange coefficient between electron and heavy-species (inversely proportional to the characteristic time for inter-particle collisions [14]), $\boldsymbol{\tau}$ represents the stress tensor for a Newtonian fluid, ε_r is effective net radiative energy emission coefficient; $\mathbf{J}_q\cdot(\mathbf{E} + \mathbf{u}\times\mathbf{B})$ represents Joule heating. In LTE models it is customarily assumed $\mathbf{E}_p \approx \mathbf{E}$ [13]. Here, $\mathbf{E}_p = -\nabla\phi_p - \partial_t\mathbf{A}$, in which ϕ_p is the effective electric potential and $\mathbf{A}$ the magnetic vector potential such that $\nabla\times\mathbf{A} = \mathbf{B}$. Similar as done in [13], our model

assumes $\nabla\cdot(\sigma\partial_t\mathbf{A})\approx 0$, since generally $\|\partial_t\mathbf{A}\| << \|\nabla\phi_p\|$ in most of the domain. A more detailed description of the model and the nomenclature used are described in [13].

The equations in table 1 can be expressed in residual form for the vector of unknowns **Y** as:

$$\mathcal{R}(\mathbf{Y}) = \underbrace{\mathbf{A_0}\partial_t\mathbf{Y}}_{\text{transient}} + \underbrace{(\mathbf{A}_i\partial_i)\mathbf{Y}}_{\text{advective}} - \underbrace{\partial_i(\mathbf{K}_{ij}\partial_j\mathbf{Y})}_{\text{diffusive}} - \underbrace{(\mathbf{S_1}\mathbf{Y}+\mathbf{S_0})}_{\text{reactive}} = \mathbf{0}, \tag{1}$$

where $\mathcal{R}$ is the residual vector, $\mathbf{A_0}$, $\mathbf{A}_i$, $\mathbf{K}_{ij}$, $\mathbf{S_1}$, $\mathbf{S_0}$ are coefficient matrices that are used to characterize the different transport processes, i and j are spatial indices, and Einstein's convention of repeated indexes has been used. The system in Eq. (1) is solved for the set of primate variables given by:

$$\mathbf{Y} = [p \;\; \mathbf{u} \;\; T_h \;\; T_e \;\; \phi_p \;\; \mathbf{A}]. \tag{2}$$

The definition of the coefficient matrices requires the evaluation of the derivatives of the thermodynamic coefficients (ρ, ρh_h, ρh_e) against the state variables (p, T_h, and T_e), which can be considered as additional material properties not encountered in LTE models [13]. In this work, thermodynamic and transport properties are expressed in terms of pressure p, electron temperature T_e, and the thermal nonequilibrium parameter $\theta = T_e/T_h$. Thermodynamic properties are computed using standard kinetic theory procedures, whereas transport properties are retrieved using a table look-procedure, as described in [13]. Material properties vary by several orders of magnitude and in a very non-linear manner due to energetic transitions such as ionization, dissociations, etc. For example, in the case of argon, the thermodynamic property $\partial\rho/\partial T_e$ varies by 2 orders of magnitude between T_e = 0.3 and 30 (kK) and by an order of magnitude between θ = 1 and 10 for $T_e \approx 10$ (kK); electrical conductivity σ increases by two orders of magnitude for the same range of θ and $T_e \approx 5$ (kK); and K_{eh} increases by ~ 8 orders of magnitude within 5 (kK) < T_e < 15 (kK). The additional complexity of material properties in NLTE models with respect to LTE leads to higher numerical stiffness, which makes NLTE simulations computationally more expensive. Thus, nonequilibrium plasma flow models require robust numerical techniques for their solution, such as those described next section.

3. Computational model

Finite Element Methods (FEMs), due to their inherent advantages as comprehensive numerical discretization approaches, particularly for the handling of unstructured partitions, are extensively used in diverse fields, including plasma flow modeling [15]. Among FEMs, the Variational Multiscale method (VMS) has demonstrated to provide a general and robust formulation for diverse types of problems, such as scalar transport, incompressible, compressible, reactive, and turbulent flows, radiation transport, magnetohydrodynamics [13], and plasma flows [16-19]. The VMS method starts with a Galerkin formulation of the problem given by Eq. (1), i.e.,

$$\int_{\Omega} \mathbf{W}\cdot\mathcal{R}(\mathbf{Y})\,d\Omega = (\mathbf{W},\mathcal{R}(\mathbf{Y}))_{\Omega} = \mathbf{0}, \tag{3}$$

where Ω is the spatial domain and $\mathbf{W}$ the weight function. Decomposing the solution field $\mathbf{Y}$ into large-scales as $\bar{\mathbf{Y}}$ (captured by the discretization grid) and small-scales $\mathbf{Y'}$ (smaller than the grid size), i.e. $\mathbf{Y} = \bar{\mathbf{Y}} + \mathbf{Y'}$, applying the same decomposition to the weight function $\mathbf{W} = \bar{\mathbf{W}} + \mathbf{W'}$, and replacing these expressions into Eq. (3), leads to two coupled problems, one for the large- and one for the small-scales. The solution of the small-scales problem can be casted as a function of the large-scales solution to lead to a single expression for the large-scales of the form:

$$(\bar{\mathbf{W}}, \mathcal{R}(\bar{\mathbf{Y}}))_{\Omega} + (\mathcal{L}^{*}\bar{\mathbf{W}}, \mathbf{Y'})_{\Omega} = \mathbf{0}, \tag{4}$$

where $\mathcal{L}$ is the transport operator obtained from $\mathcal{R}(\mathbf{Y}) = \mathcal{L}\mathbf{Y} - \mathbf{S}_0$ and the superscript * denotes the adjoint operator. The small-scales are approximated algebraically as $\mathbf{Y'} \approx -\boldsymbol{\tau}\mathcal{R}(\bar{\mathbf{Y}})$, where $\boldsymbol{\tau}$ is the so-called intrinsic time scales matrix such that $\boldsymbol{\tau} \approx \mathcal{L}^{-1}$. The final VMS formulation is given by [13, 14]:

$$\begin{aligned} \mathbf{R}_h(\mathbf{Y}_h) = {} & (\mathbf{N}, (\mathbf{A_0}\partial_t + \mathbf{A}_i\partial_i - \mathbf{S_1})\mathbf{Y}_h - \mathbf{S_0})_{\Omega} + (\partial_i \mathbf{N},\ \mathbf{K}_{ij}\partial_j \mathbf{Y}_h)_{\Omega} + \\ & + ((\mathbf{A}_i^{\mathsf{T}}\partial_i + \mathbf{S_1}^{\mathsf{T}})\mathbf{N}, \boldsymbol{\tau}((\mathbf{A_0}\partial_t + \mathbf{A}_i\partial_i - \mathbf{S_1})\mathbf{Y}_h - \mathbf{S_0}))_{\Omega'} + (\partial_i \mathbf{N}, \mathbf{K}_{ij}^{DC}\partial_j \mathbf{Y}_h)_{\Omega'} = \mathbf{0}. \end{aligned} \tag{5}$$

The first two terms on the right side of Eq. (5) represent the Galerkin formulation; the third term represents the modeling of the small-scales, and the last term represents the discontinuity-capturing operator, included to add robustness to the formulation in the presence of large solution gradients. $\mathbf{R}_h$ represents the final discrete residual, counterpart to $\mathcal{R}$, which is obtained by setting $\bar{\mathbf{W}}$ as the finite element basis function $\mathbf{N}$ and $\bar{\mathbf{Y}}$ as the actual finite element solution field $\mathbf{Y}_h$.

The nonlinear algebraic-differential system given by Eq. (5) is solved by a fully-implicit second-order accurate predictor multi-corrector time-stepper together with a globalized Newton-Krylov method. Details about the numerical solution approach are found in [13].

4. Simulation set-up

Two domain configurations are studied, which are shown in Figure 3. Figure 3(a) presents the configuration used by Benenson *et al* [8], having a relatively low aspect ratio and circular cross-section electrodes, which will be referred hereinafter as the weak-arc configuration; and figure 3(b) used by Kelkar *et al* [1], having a larger aspect ratio and square cross-section electrodes, which will be referred hereinafter as the strong-arc configuration. Figure 3 shows the geometrical domain, characteristic dimensions, boundary sides, as well as representative depictions of the arc plasma.

The geometrical dimensions for the weak-arc configuration are L_x x L_y x L_z = 6.64 (mm) x 14 (mm) x 25.3 (mm) and the cathode and the anode diameters are 2 (mm) and 5 (mm), respectively. The geometrical dimensions for the strong-arc configuration are: L_x x L_y x L_z = 2 (mm) x 15 (mm) x 30 (mm), and the square electrode dimensions are of size 3 (mm) x 3 (mm). (Note: $L_x = H$ in Figure 2.)

The set of boundary conditions used in the simulations of both configurations are listed in table 2. A normal zero pressure gradient is used at all boundaries except at 'outflow_z', where a value of

pressure equal to 1 (atm) is imposed. The gas velocity at the inflow is specified by a parabolic profile $\mathbf{u_i}$ that depicts a fully-developed laminar gas flow stream, i.e. $\mathbf{u_i} = [u_{ix}\ u_{iy}\ u_{iz}]^T = [\ 0\ 0\ U_{imax}(1 - (x/H))(x/H)\ ]^T$. The no-slip condition is applied to the electrode surfaces and to the wall surrounding them (i.e., the anode, the cathode, and the walls).

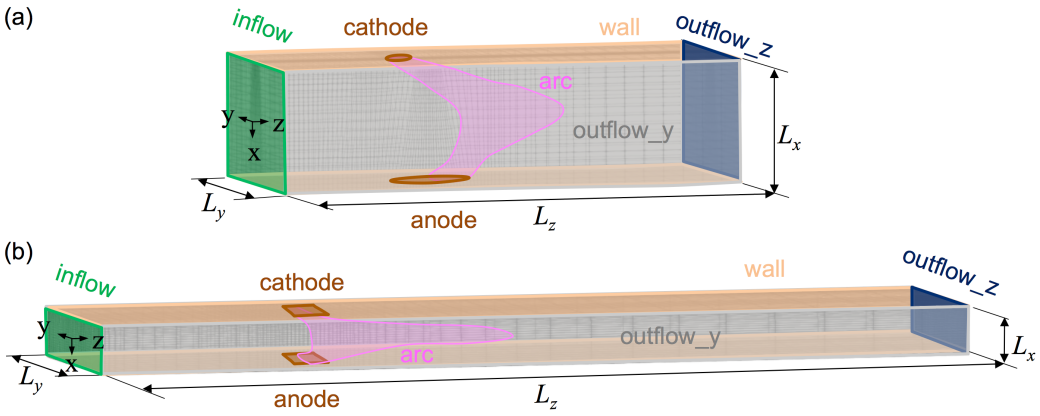

Figure 3. Computational domain and boundaries for the arc in crossflow simulations.

Table 2. Set of boundary conditions for the arc in crossflow.

Boundary	p	$\mathbf{u}$	T_h	T_e	ϕ_p	$\mathbf{A}$
inflow	$\partial_n p = 0$	$\mathbf{u} = \mathbf{u_i}$	$T_h = T_0$	$T_e = T_0$	$\partial_n \phi_p = 0$	$\mathbf{A} = \mathbf{0}$
anode	$\partial_n p = 0$	$\mathbf{u} = \mathbf{0}$	$-k_h \partial_n T_h = h_w (T_h - T_w)$	$\partial_n T_e = 0$	$\phi_p = 0$	$\partial_n \mathbf{A} = \mathbf{0}$
cathode	$\partial_n p = 0$	$\mathbf{u} = \mathbf{0}$	$T_h = T_c$	$\partial_n T_e = 0$	$-\sigma\ \partial \phi_p = J_{qcath}$	$\partial_n \mathbf{A} = \mathbf{0}$
wall	$\partial_n p = 0$	$\mathbf{u} = \mathbf{0}$	$-k_h \partial_n T_h = h_w (T_h - T_w)$	$\partial_n T_e = 0$	$\partial_n \phi_p = 0$	$\partial_n \mathbf{A} = \mathbf{0}$
outflow_z	$p = p_\infty$	$\partial_n \mathbf{u} = \mathbf{0}$	$\partial_n T_h = 0$	$\partial_n T_e = 0$	$\partial_n \phi_p = 0$	$\partial_n \mathbf{A} = \mathbf{0}$
outflow_y	$\partial_n p = 0$	$\partial_n \mathbf{u} = \mathbf{0}$	$\partial_n T_h = 0$	$\partial_n T_e = 0$	$\partial_n \phi_p = 0$	$\partial_n \mathbf{A} = \mathbf{0}$

The heavy-species temperature is specified over the cathode surface using a parabolic profile, i.e.,

$$T_c = T_{c0}(1 - (y / y_{cath})^2 - ((z - z_{off}) / z_{cath})^2), \tag{6}$$

where y and z are the spatial coordinates, y_{cath} and z_{cath} are characteristic lengths set equated to 1 (mm) and 1.5 (mm) for the weak-arc and the strong-arc configurations, respectively, and z_{off} refers to the offset distance between the origin and the center of the cathode. The cathode temperature T_c is maximum at the cathode center with the value of T_{c0} set close to the melting point for Tungsten [8], and a minimum value at the cathode boundaries close to the wall-cooling reference temperature T_w.

Convective heat transfer driven by the heavy-species temperature is imposed over the anode and wall surfaces using a convective heat transfer coefficient h_w and reference wall temperature T_w, i.e. $-k_h \partial_n T_h = h_w(T_h - T_w)$, where n represents the wall-normal direction. A zero normal gradient condition for the electron temperature is imposed over all boundaries except the inflow (i.e. the inflow gas is assumed in LTE).

A current density J_{qcath} profile is specified over the cathode boundary following a quasi-Gaussian distribution, i.e.,

$$J_{qcath} = J_{qcath0} \exp(-(r / R_c)^{n_c}), \tag{7}$$

where $r = (x^2 + y^2)^{\frac{1}{2}}$ is the radial coordinate; n_c, R_c and J_{qcath0} are parameters chosen such to impose a value of total current $I_{tot} = \int J_{qcath} dS$, where the integral is over the cathode domain surface.

In table 2, the common boundary conditions applied to both the configurations are: $p_\infty = 1.01325 \cdot 10^5$ (Pa), $h_w = 2.0 \cdot 10^4$ (Wm^{-2}K^{-1}), representative of forced water cooling over a metal surface [20], and $\mathbf{u_0} = [\ 0\ 0\ U_i\ ]$ with a parabolic distribution such that $U_i = U_{imax}$ at the centre and $U_i = 0$ at the edges. The additional boundary conditions applied are specific for each configuration are as follows: *weak-arc*: $U_{imax} = 0.5$ (ms^{-1}), inlet temperature $T_0 = 300$ (K), reference cooling temperature $T_w = 300$ (K), $T_{c0} = 3000$ (K), and $I_{tot} = 17$ to 34 (A) enforced by setting $J_{cath0} = 0.24025 \cdot 10^8$ to $0.4805 \cdot 10^8$ (Am^{-2}), and using $n_c = 3$, and $R_c = 0.5$ (mm); *strong-arc*: $U_{imax} = 1.17$ (ms^{-1}) to 117 (ms^{-1}), $T_0 = 500$ (K), $T_w = 1000$ (K), $T_{c0} = 3000$ (K), and $I_{tot} = 7$ to 435 (A) using $J_{cath0} = 0.04095 \cdot 10^8$ to $2.423 \cdot 10^8$ (Am^{-2}) using $n_c = 6$, and $R_c = 0.8$ (mm).

5. Simulation results and model validation

5.1. Representative results

Representative 3D steady-state solution fields through the *x-z* plane for the two configurations are presented in figures 4 and 5. The operating conditions for the weak-arc configuration results in figure 4 are: $I_{tot} = 34$ (A) and $U_{imax} = 0.5$ (ms^{-1}), whereas those for the strong-arc results in figure 5 are: $I_{tot} = 200$ (A) and $U_{imax} = 100$ (ms^{-1}).

For both cases, the value of pressure increases near the electrodes and decreases to atmospheric pressure at the outflow. The local pressure at the cathode is higher than that near the anode due to the magnetic pressure caused by the constricted current path. The overall pressure difference is significantly higher in the strong-arc configuration than in the weak-arc configuration due to the higher magnitude of total current. The constricted current path near the cathode produces localized Joule heating and electromagnetic pumping leading to the formation of a cathode jet, which can be observed in the distributions of velocity magnitude $||\mathbf{u}||$, especially for the strong-arc configuration.

The higher velocities obtained in the simulations are primarily due to the variation of material properties with T_h and T_e. At higher temperatures, mass density decreases, causing local expansion and acceleration of the plasma cathode jet. However, the viscosity partially restricts the increase in velocity magnitude for $T_h < 15$ (kK); but for $T_h > 15$ (kK), both, viscosity and densities decrease, causing a significant increase in velocity. The obtained velocity magnitudes are comparable to those obtained with LTE models, e.g., Kelkar and Heberlein reported axial velocities of up to 1300 (ms^{-1}) [1], whereas for the present NLTE model, the maximum axial velocity is ~ 1560 (ms^{-1}).

The solutions fields for the heavy-species T_h and the electron T_e temperatures are indicative of the arc shape. The magnitude of total current I_{tot} induces distinct arc attachments at the anode (i.e., constricted/spot or diffuse [21]); particularly, the anode attachment is relatively diffuse in the weak-arc configuration compared to that for the strong-arc. Additionally, the imposed current density profile J_{qcath} attaches the arc to the center of the cathode, leading to relatively minor sensitivity to the inflow gas flow compared to the anode, which shows upstream or downstream edge attachment (the arc is attached to the downstream edge of the anode in the strong-arc configuration). The arc shape is primarily a result of the imbalance between the self-induced electromagnetic force and the gas drag force due to impinging of the cold gas on the hot arc. The neglect of the electrode sheaths in the model is expected to have a minor effect on the arc shape due to their small extent compared to the extent of the flow domain and of the plasma – gas flow interphase. The adequate modeling of the electrode-plasma interaction region within 3D flow simulations involves significantly larger model complexity and computational cost, and is an active area of research [22-24].

The arc is cusp-shaped for the weak-arc case (figure 4(c)), whereas it appears as bow-shaped for the strong-arc one (figure 5(c)) due to stronger advective transport. The deviation from thermal equilibrium is clearly noticeable in the weak-arc configuration, as observed by contrasting the distribution of T_h and the more diffuse distribution of T_e (figure 4 (c) and (d)). Higher currents and inflow velocities cause varying degrees of thermal nonequilibrium, i.e. diffuse near the cold-gas inlet leading to electron pre-heated zones and relatively constricted near the arc-plasma interface region. The degree of deviation from LTE is discussed in greater detail in section 5.3.

The electric potential ϕ_p distribution, as seen in figure 4(e) and figure 5(e), shows a somewhat abrupt change for the strong-arc configuration compared to the weak-arc one due to the markedly stronger arc-gas flow interaction. Characterization of the arc-gas flow interaction is presented in Section 6. The distribution of magnetic potential for both configurations shows that the electromagnetic force is primarily driven by the distribution of current density following the arc shape and gradient of electric potential.

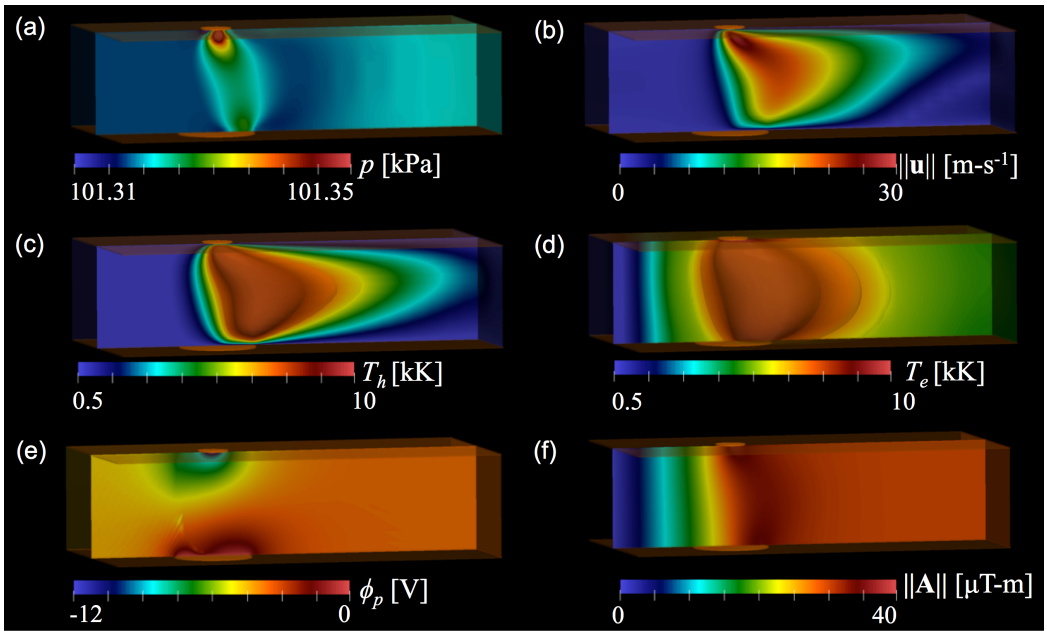

Figure 4. Steady-state solution fields for the weak-arc configuration: (a) pressure, (b) velocity magnitude, (c) heavy-species temperature, (d) electron temperature, (e) electric potential and (f) magnetic vector potential. Conditions: I_{tot} = 34 (A) and U_{imax} = 0.5 (ms^{-1}).

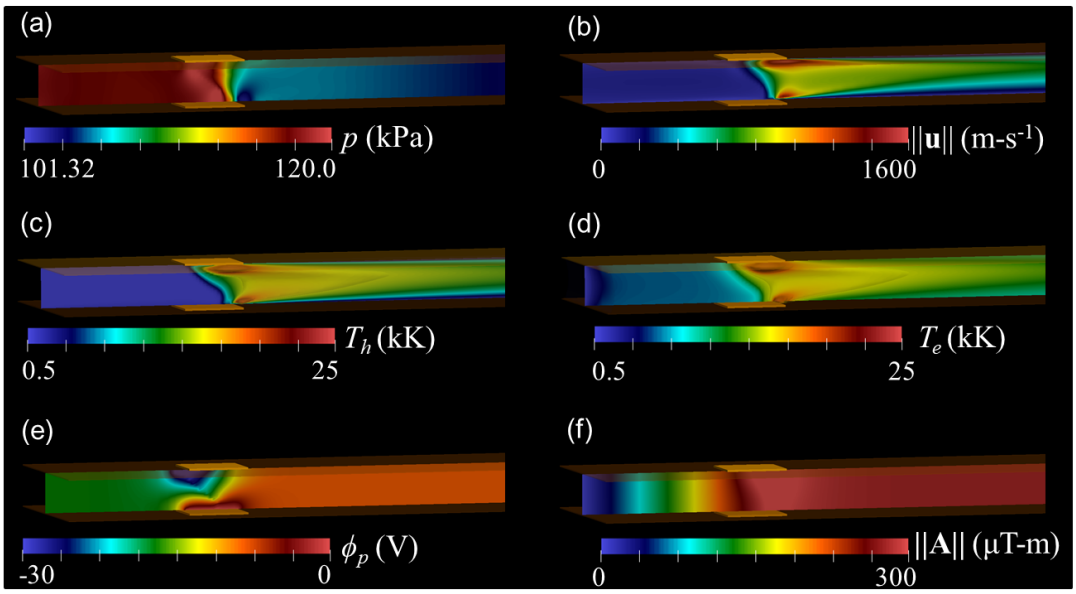

Figure 5. Steady-state solution fields for the strong-arc configuration: (a) pressure, (b) velocity magnitude, (c) heavy-species temperature, (d) electron temperature, (e) electric potential and (f) magnetic vector potential. Conditions: I_{tot} = 200 (A) and U_{imax} = 100 (ms^{-1}).

The obtained results in figure 4 and figure 5 are obtained by using the VMS model given by equation (5), which has not been devised to account for highly nonlinear inter-scale interactions, as needed to simulate flow turbulence. Additionally, the mathematical model (table 1) does not include any turbulence model (of the Reynolds Averaged Navier-Stokes (RANS) type). Turbulent effects in

the arc in crossflow can be expected near the arc-plasma interface, due to large temperature gradients (from 10^4 (K/mm) to 10^6 (K/mm)) [25], leading to rapid heating and gas acceleration. To model these effects using the VMS framework, the small-scale term in Eq. (5) should be modified to account for the non-linearity of the small-scales and the mesh discretization should be small enough to capture these variations. However, the current discrete model and mesh resolution cannot ensure capturing turbulent flow features. The use of VMS methods for turbulent flow simulations, in what are traditionally referred as residual-based VMS Large-Eddy Simulation (VMS-LES) approaches, has been reported for diverse flows [26, 27] and recent efforts for nonequilibrium plasma flows in [28].

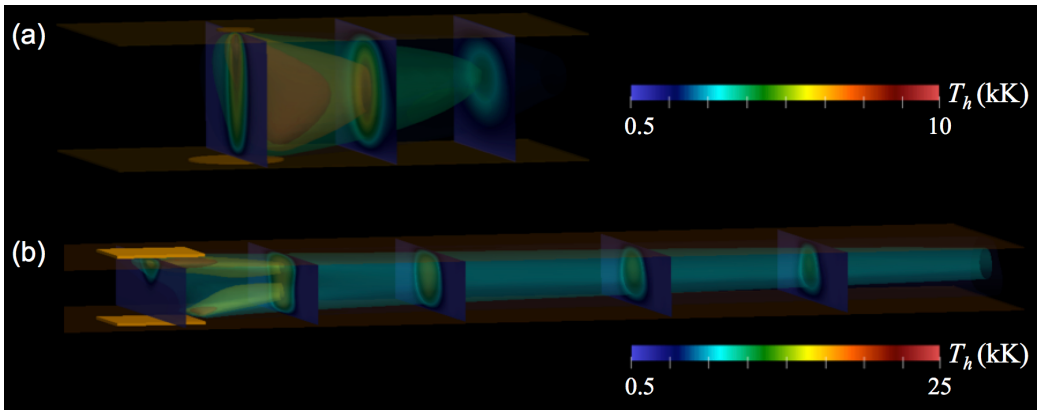

Figure 6. 3D solution fields of heavy-species temperature distribution T_h: iso-surfaces and perpendicular slices for (a) the weak-arc configuration (I_{tot} = 34 (A) and U_{imax} = 0.5 (ms^{-1})) and (b) the strong-arc configuration (I_{tot} = 200 (A) and U_{imax} = 100 (ms^{-1})).

The shape of the arc along planes perpendicular to the gas-flow direction (x-y), together with T_h iso-surfaces, can be observed in figures 6(a) and 6(b) for the weak- and the strong-arc configurations, respectively. These results are representative of the spatial evolution of the plasma within the 3D domain. The relatively minor deflection of the arc in the weak-arc configuration translates into a single elongated plasma region along the slices in figure 6(a). In contrast, the dramatic arc deflection in the strong-arc configuration is evidenced by the separated plasma regions in the slice closest to the electrodes in figure 6(b). These regions get joined downstream forming a cohesive afterglow region.

5.2. Model validation

The two-temperature plasma flow model is validated against the experimental results by Benenson *et al* [8], corresponding to the weak-arc configuration (see figure 3(a) and results in figure 4). Figure 7 compares the obtained heavy-species and electron temperature distributions obtained with the two-temperature NLTE model along the mid-cross section plane against the corresponding experimentally-determined LTE temperature distribution reported in [8]. In that figure, the gas flow is directed towards the positive z-axis.

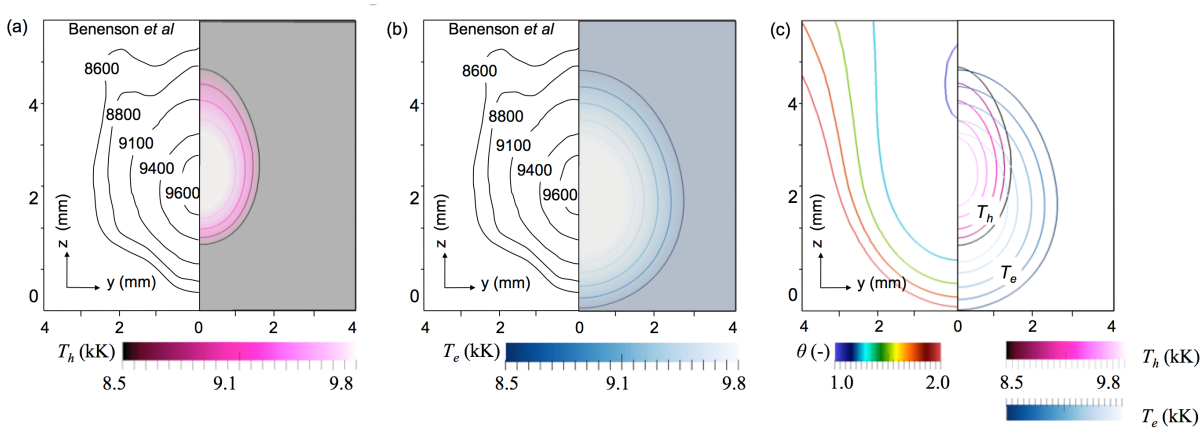

Figure 7. Validation of the two-temperature (NLTE) arc in crossflow model in the mid-cross section plane: (a) (*left*) LTE temperature determined experimentally by Benenson *et al* [8] and (*right*) T_h from the model; (b) (*left*) experimental LTE temperature and (*right*) T_e from the model; (c) (*left*) $\theta = T_e/T_h$ and (*right*) superposed contour lines for T_h and T_e.

The maximum heavy-species and electron temperatures obtained with the two-temperature model are: T_{hmax} = 9807 (K) and T_{emax} = 10160 (K), respectively. These values are contrasted against the maximum experimental (LTE) temperature $T_{max\text{-}exp}$ = 9685 ± 300 (K), where the uncertainty is due to complications in determining brightness temperature and calibrating the tungsten filament [8]. Comparison of these values indicate that $T_{max\text{-}exp} < T_{hmax} << T_{emax}$, which appears consistent with the fact that the experimental results were determined assuming LTE, and therefore may overestimate the energy content carried by the plasma. This hypothesis is also corroborated by the more diffuse distribution of the experimental temperature T_{exp} distribution with respect to both, T_h and T_e and that all of them approximately present the same location for the arc core (location of maximum temperatures).

The distributions of T_h and T_e in figure 7(a) and 7(b) appear markedly dissimilar upstream (arc – gas flow interface, constricted T_h and diffuse T_e) while they seem to match in the downstream region. This result indicates significant deviation from thermal equilibrium at the gas-plasma interaction zone, as shown in figure 7(c), where the degree of nonequilibrium $\theta = T_e/T_h$ (*left*) is contrasted against the T_h and T_e distributions (*right*). The high nonequilibrium in the arc – gas flow interface is due to deflection of arc caused by drag acting over the heavy-species and the rapid radial diffusion of electrons caused by local heating [29].

Additionally, figure 7(c) shows a region of deviation from thermal nonequilibrium at the arc-core, near the location of maximum temperature. The degree of deviation θ varies from 1.0 to 1.03 near to the arc-core and hence this region can be reasonably approximated as being in LTE. Nevertheless, significant deviations from thermal equilibrium are observed in the periphery of the arc due to its interaction with the stream of impinging gas flow.

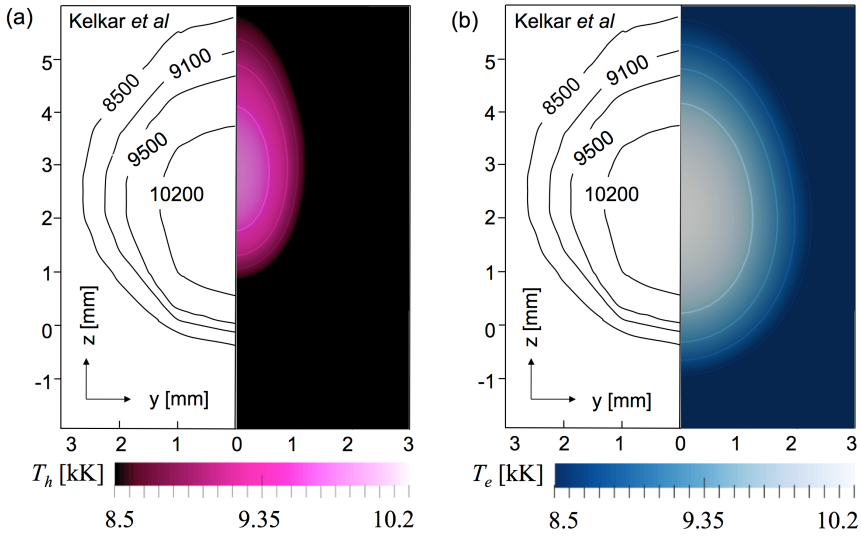

Figure 8. Comparison of NLTE against LTE results for the weak-arc configuration: mid cross-section distribution of (a) T_h and (b) T_e, (*left*) LTE results from Kelkar *et al* [1] and (*right*) NLTE results.

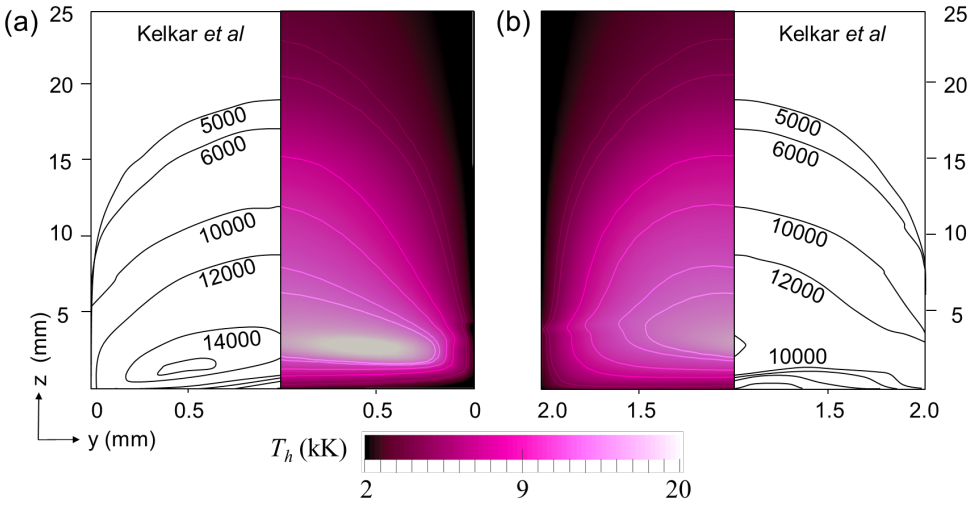

Figure 9. Comparison of NLTE against LTE results for the strong-arc configuration: axial distribution of T_h against the LTE results in [1] for the (a) cathode and (b) anode regions.

The two-temperature NLTE arc in crossflow model is also validated with the LTE model by Kelkar and Heberlein [1] for the two studied configurations. Validation results for the weak-arc configuration are shown in figure 8 and for the strong-arc one in figure 9. Figure 8 shows the distribution of T_h and T_e and the LTE temperature T along a mid-plane cross-section, as reported in [1], where the flow is in the positive z-direction. The weak-arc results show that the two-temperature model produces higher deflection of the arc, as given by the contours of T_h, while the more diffusive characteristics of the T_e distribution lead to better agreement with the distribution of T. Overall, the distributions of T_h and T_e seem to enclose that for T, as expected from a total energy conservation standpoint.

Similarly, figure 9 shows the distribution heavy-species temperature T_h and the LTE temperature T in the plane across the extent of the arc [1]; frame (a) compares the distributions near the cathode region and frame (b) near the anode region. As in the previous figures, the gas flow is in the positive z-direction. The NLTE results show significantly higher values of T_h compared to those of T by the LTE model, particularly near the cathode. Such result is consistent with the approximately larger arc deflection observed in the NLTE model, which should lead to arc constriction and therefore to higher temperatures to maintain the electric current flow. The distribution of electron temperature T_e (not shown in the figure) presents a similar behavior to that discussed for the results in figures 5 and 7.

5.3. Effect of total current and velocity

Figure 10 and figure 11 show the effect of imposed total current I_{tot} and inflow velocity U_{imax} on the distributions of T_h, T_e, and the nonequilibrium distribution $\theta = T_e/T_h$ for the weak- and strong-arc configurations, respectively. Consistent with results by other authors (e.g., [1, 9, 11]), the NLTE model results show that increasing I_{tot} leads to increased arc shielding (i.e. larger arc extent, as seen by contrasting figure 10(a) and 10(b)) due to greater Joule heating; while increasing U_{imax} causes greater arc constriction (i.e. smaller arc cross-section, as appreciated by comparing figure 11(a) and 11(b)) due to greater energy losses. Additionally, it can be observed that increasing I_{tot} leads to a progressive change of the arc shape from bow- to cusp-shaped, while increasing U_{imax} changes the arc shape from cusp- to bow-shaped. The distribution of θ shows little or no effect with increasing I_{tot} (figure 10) and a somewhat more pronounced effect with increasing U_{imax} (figure 11).

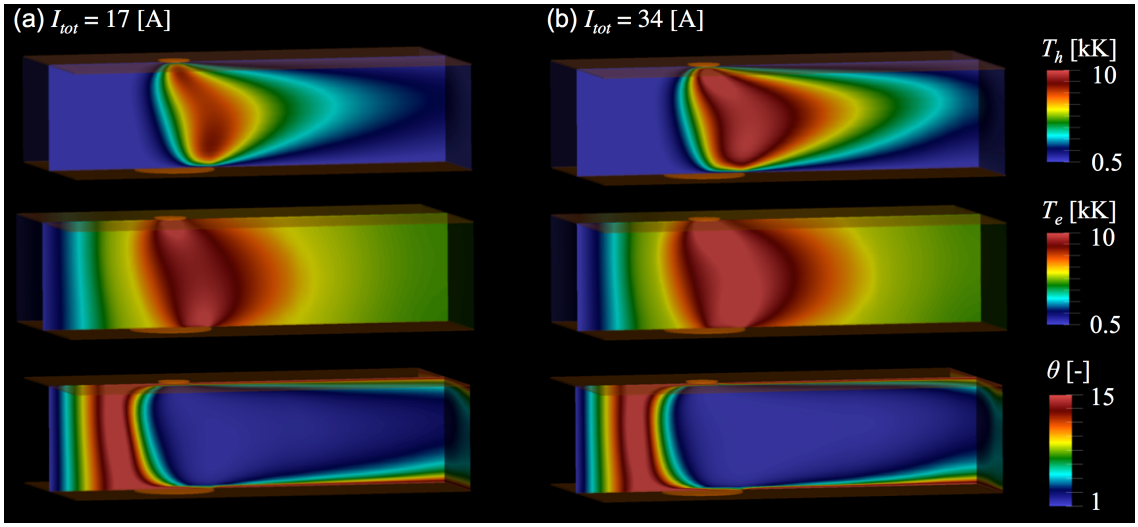

Figure 10. Effect of total current on heavy-species temperature, electron temperature, and nonequilibrium parameter for U_{imax} = 0.5(ms^{-1}), (a) I_{tot} = 17 (A) and (b) I_{tot} = 34 (A).

The observed effects of imposed current and inflow velocity on the arc are informative, but of limited applicability to assist equipment design and process optimization. For example, the

conclusions from the previous analysis are not amenable for their direct extension to other gases or geometrical configurations (e.g. inter-electrode spacing) given that I_{tot} and U_{imax} do not constitute an approximately complete set of parameters for the problem. A more effective characterization of the arc in crossflow has to be based on an appropriate set of dimensionless parameters that can encapsulate the major components of the system, as addressed in the next section.

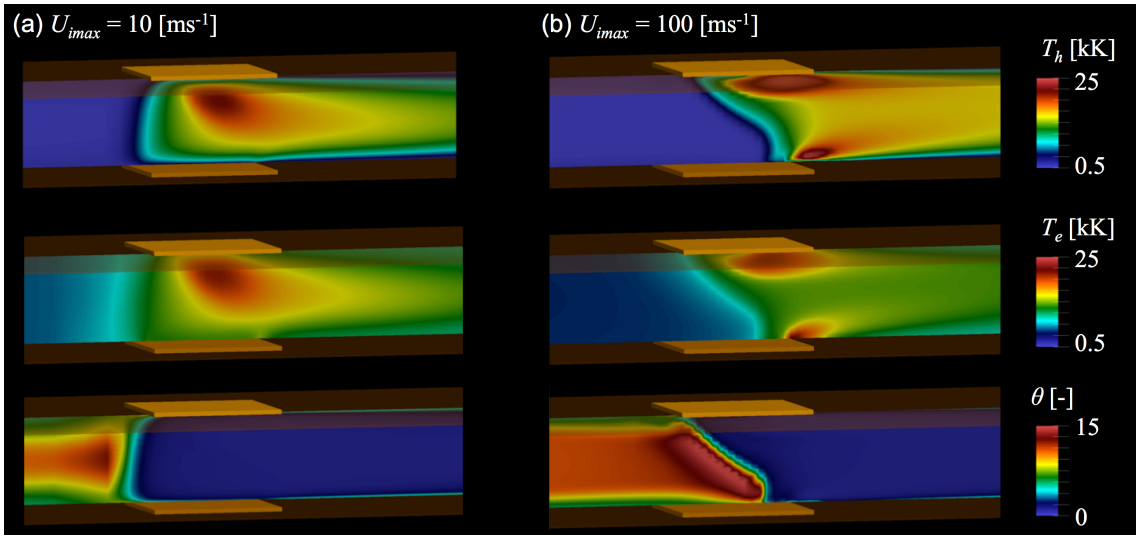

Figure 11. Effect of imposed velocity on heavy-species temperature, electron temperature, and nonequilibrium parameter for I_{tot} = 200 (A), (a) U_{imax} = 10 (ms^{-1}) and (b) U_{imax} = 100 (ms^{-1}).

6. Parametric characterization of the arc in crossflow

6.1. Dimensionless parameters and main characteristics

The shape and characteristics of the arc are mainly the results of the competing effects produced by the supplied electrical energy input (Joule heating) and the energy lost to the stream of working gas (convective cooling). The dominant mechanism is the one that has the least root-mean-square deviation in the arc discharge characteristics [30]. These effects depend on the set of parameters specifying the problem, such as total current, inflow velocity, inter-electrode spacing, gas type, etc. (figure 2). The set of controlling parameters can be analyzed more effectively through the specification of appropriate non-dimensional numbers. A detailed set of non-dimensional numbers to characterize various plasma configurations, such as magnetic/self-propelled arcs, co-axial electrode plasma arcs, wall-stabilized arcs, free burning arcs, parallel and crossflow arcs, are presented by Yasko *et al* [31]. For the arc in crossflow, two main non-dimensional numbers are: the Reynolds number *Re* and the Enthalpy number Π_h. The Reynolds number is given by the ratio of estimates of the magnitude of advective transport to that for diffusive transport, and hence characterizes the relative strength of the stream of gas flow (i.e. the larger *Re* is, the greater the bulk transport by the flow). The Enthalpy number is given by the ratio of estimates of the magnitude of energy transported

by advection to that for the electrical energy input, and therefore characterizes the strength (or weakness) of the arc (i.e. the larger the inverse of Π_h, the more robust the arc is). Therefore, for high values of Π_h^{-1}, the electromagnetic forces overcome the flow drag forces, which cause increased heating, better-established electrode attachments, and a more stable arc column. The dimensionless numbers *Re* and Π_h are defined by [32]:

$$Re = \frac{\rho_i U_{i\max} H}{\mu_i} \quad \text{and} \quad \Pi_h = \frac{\sigma_r h_r \rho_r U_{i\max} H^3}{I_{tot}^2}, \tag{8}$$

where the subscripts '*r*' denote the value of a given property evaluated at some reference temperature (set equal to 16.7 kK in the present work) [32] and '*i*' denote values evaluated at the inlet conditions.

The phenomenological characterization of the arc in crossflow is performed by computational simulations of a total of 19 cases shown in table 3. The distributions of T_h for these cases are plotted in figure 12 over a *Re*-Π_h^{-1} chart for the range $0 < Re < 10000$ and $2 < \Pi_h^{-1} < 350$. The distribution of cases is not uniform such to include the cases studied by Kelkar and Heberlein [1] and to emphasize the regions with more drastic changes in the solution fields. The variation of Reynolds and the Enthalpy numbers among the cases are accommodated by modifying the inlet velocity $U_{i\max}$ and the imposed current I_{tot}.

Table 3. *Re* and Π_h^{-1} numbers for the computational characterization of the arc in crossflow.

Case No.	1	2	3	4	5	6	7	8	9	10
$10^3 Re$	0.5	3	7.5	10	0.1	3	7.5	10	2.5	7.5
Π_h^{-1}	2	2.5	2.5	2	10	6.67	6.67	10	87.5	87.5
Case No.	11	12	13	14	15	16	17	18	19	
$10^3 Re$	8.63	0.5	5	10	2.5	7.5	0.1	2.16	10	
Π_h^{-1}	85.4	200	175	200	262	262	10	344	350	

The results in figure 12 show that the arc shape changes from cusp-shaped to bow-shaped with increasing *Re* (from case 1 to case 4 or from case17 to case19) or for a reduction in Π_h^{-1} (from case 17 to case 1, or from case 19 to case 4). The curvature and deflection of the arc are largest for the maximum *Re* and minimum Π_h^{-1} studied (i.e. bottom-right corner of figure 12). This behavior is consistent with reports in the literature [8, 9]. The results also show the increase in T_h with increasing Π_h^{-1}, as expected due to larger values of I_{tot}; but also, with increasing *Re*, due to the stronger cooling by the gas flow which leads to higher temperatures to maintain current continuity. This result is

indicative of the balance between electrical energy input and its dissipation by the stream of gas, and supports the need for considering the parameters *Re* and Π_h^{-1} simultaneously for the characterization of the arc in crossflow. Finally, the arc attachment at the farthest downstream edge of the anode can be observed for increasing values of *Re* and lower values of Π_h^{-1}.

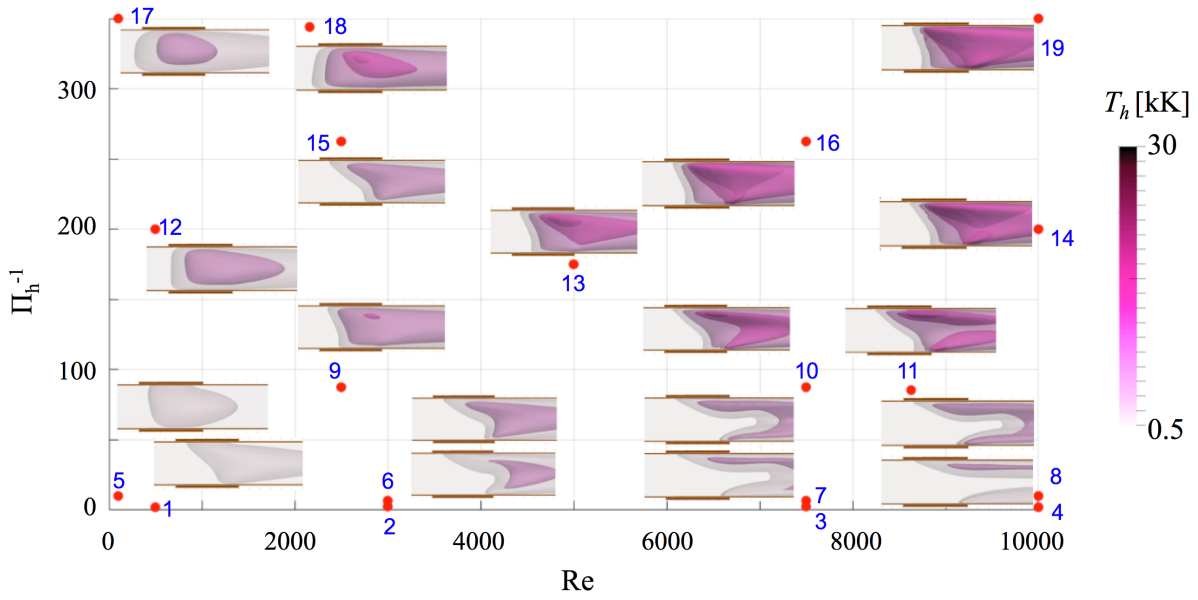

Figure 12. Characterization of the arc plasma shape: iso-surfaces of T_h = 2, 8, 15, 20 (kK) as function of the Reynolds number *Re*, representative of the gas flow strength, and the inverse Enthalpy number Π_h^{-1}, indicative of the arc strength. The red dots indicate conditions for each simulation.

The steady-state results in figure 12 were obtained by time-dependent simulations until consistent time-averaged results were obtained (i.e. simulations were run for an approximate extent of ~ 4 characteristic transit times given by L_z/U_{imax}). The obtained simulations have shown various solution trends (distributed over the *Re*-Π_h^{-1} map) such as steady, semi-steady (i.e. steady with small-amplitude random fluctuations), quasi-periodic and periodic, as given by the localized temperature and voltage drop temporal signals. Simulations with *Re* > 7000 and Π_h^{-1} > 200 (cases 14, 16, and 19) present severe pressure fluctuations associated with high values of T_h (~ 30 kK) at the near-cathode regions. For these cases, the simulations showed frequent convergence failures due to large temperature and velocity gradients in the plasma-electrode and plasma-wall regions, potentially associated with coarse-sized elements in the discretization mesh. Additionally, obtaining converged results for the high *Re* and Π_h^{-1} cases required more timesteps with smaller step size and more iterations per timestep, adding to the overall computational cost. The high-pressure sensitivity and large temperature and velocity gradients are indicative of complex plasma flow behaviors, which can potentially lead to instability

and turbulence [33]. A quantitative study of the plasma dynamics under such conditions is beyond the scope of this paper and will be addressed in future work.

Representative characteristics of the arc in crossflow are presented in a Re-Π_h^{-1} in figure 13, namely: maximum electric potential drop $|\phi_{\max}|$ (V), maximum electric power $P_{\max} = I_{tot}|\phi_{\max}|$ (W), and the relative change in the nonequilibrium parameter θ_{rel} defined as:

$$\theta_{rel} = (\theta_{\max} - \theta_{ref})/\theta_{ref}, \tag{9}$$

where θ_{max} is the maximum value of θ and θ_{ref} is a reference value equal to 7 representing the least value (case 5) of the maximum degree of nonequilibrium obtained from the 19-simulations set. The results in figure 13 show that, as Re is increased or Π_h^{-1} is decreased, the length of the current path increases, causing a rise in electric potential, as seen in figure 13(a). The total power consumed increases with I_{tot}, which added to the behavior of $|\phi_{\max}|$, leads to the highest level of arc power to be found in the top-right corner of the Re-Π_h^{-1} map, as seen in figure 13(b). Finally, the degree of thermal nonequilibrium degree as given by θ_{rel} and shown in figure 13(c) indicates that higher nonequilibrium is observed for larger values of Re and Π_h^{-1}, that is, with increasing the relative strength of arc – gas flow interaction. Such behavior was not clearly observed in the results as a function of U_{imax} and I_{tot} presented in figures 10 and 11.

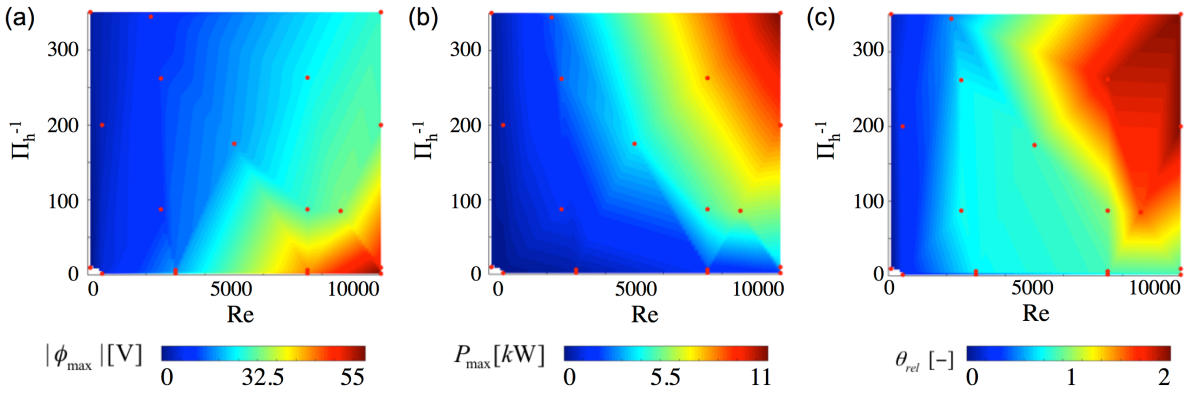

Figure 13. Arc in crossflow characterization map: (a) total voltage drop $|\phi_{\max}|$, (b) arc power $P_{\max}$, and (c) relative nonequilibrium parameter θ_{rel} as a function of Re and Π_h^{-1}.

Non-dimensional numbers such as Re and Π_h are often referred to as 'generalized inputs' given that they can be defined prior to evaluating the flow [31]. These arguments can be used to determine 'generalized outputs', such as the non-dimensional velocity $\hat{u} = \|\mathbf{u}\|/U_{i\max}$ and the non-dimensional electric potential $\hat{\phi} = \sigma_0 V_p H / I_{tot}$. To validate the use of Re and Π_h as the main non-dimensional numbers for the arc in crossflow, different solution domains, and electrode shapes are analyzed for the same generalized inputs, i.e. Re = 143 and Π_h^{-1} = 3.33, in figure 14. The results in figure 14 show that

the distributions of $\hat{u}$ and $\hat{\phi}$ are comparable (both in magnitude and distribution) irrespective of the inter-electrode distance and the electrode shape. Thus, *Re* and Π_h are appropriately considered as the main controlling parameters for the arc in crossflow.

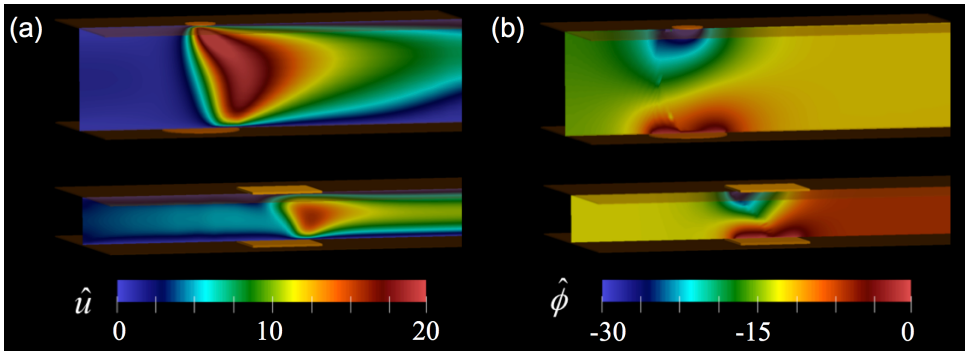

Figure 14. Common *Re* and Π_h^{-1} plasma flow simulations (*Re* = 143 and Π_h^{-1} = 3.33): Contours of (a) non-dimensional velocity and (b) non-dimensional electric field for different inter-electrode distance and electrode shapes.

6.2. Plasma front and characteristic thermal lengths

The plasma – gas flow interaction region in the arc in crossflow is somewhat analogous to the interaction of a flame with a stream of oxidizer in combustion systems. Both systems depict a rapid increase in temperature in a very small distance; in flames due to the rapid release of chemical energy, whereas in arcs due to the electric current flow and associated Joule heating. In combustion systems, such distance is customarily referred as the flame front thickness [34], which separates the burnt and unburnt zones. For arc plasma systems, an analogous plasma front thickness can be defined such that it separates the non-ionized (gas) and ionized (plasma) zones. These regions are typically pressure-sensitive [35] and exhibit large material property variations and marked nonequilibrium.

In analogy to combustion fronts, a characteristic plasma front thickness δ can be defined by:

$$\delta = \frac{(T_{ref} - T_i)}{\| \nabla T \|}, \tag{10}$$

where $\| \nabla T \|$ represents the temperature gradient, T_{ref} a reference temperature characteristic of the type of plasma gas, set equal 16.7 (kK) for the argon plasma in the current study, and T_i is the inlet gas temperature (representative of the stream of working gas). The thickness δ given by Eq. (10) can be interpreted as the distance in which the temperature of the inlet gas increases to the value T_{ref}. It can be expected that the stronger the gas-plasma or gas-flame interaction, the smaller the front thickness δ. Moreover, given the smallness of δ, the use of its inverse δ^{-1} (i.e. a semi-dimensional temperature gradient) can be more practical for the analysis of the plasma front.

An additional aspect in the analysis of plasma – gas flow interactions is the role of thermodynamic nonequilibrium, i.e. the temperature gradients of both, heavy-species and electrons, need to be considered. Given the high degree of heating characteristic of thermal plasmas and the more diffuse nature of the electron temperature distribution, the gradient of heavy-species temperature is arguably the most appropriate for the estimation of the plasma front thickness in arcs.

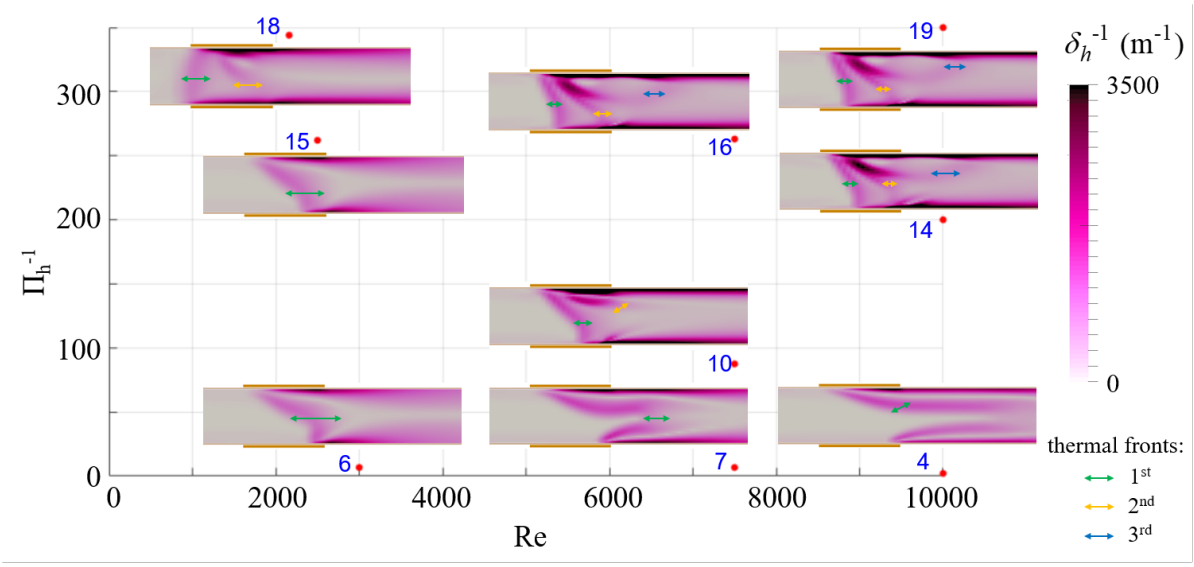

Figure 15. Characteristic plasma front length for heavy-species as function of *Re* and Π_h^{-1}. The arrows indicate the approximate thickness of the different thermal plasma fronts.

Figure 15 shows the inverse of the heavy-species plasma front thickness δ_h^{-1}, i.e. $\|\nabla T_h\|/(T_{ref}-T_g)$ for representative cases within the *Re* - Π_h^{-1} map. The distribution of δ_h^{-1} across the solution domain shows several intermittent regions, the first three of which are explicitly indicated in figure 15. The first gradient thickness is representative of the plasma – gas flow interaction region, whereas the second and third thickness, of the structure of the plasma, such as thermally reactive zones. The non-dimensional numbers, *Re* and Π_h^{-1} greatly influence the magnitude of the thermal gradient δ_h^{-1}. The thickness of the 1st thermal gradient (the arc – gas-flow interface) changes as follows: as *Re* is increased (e.g. from case 6 to case 7 or from case 7 to case 4), nonuniformity in gradient profile is developed (i.e., the magnitude decreases at the arc core but increases near the electrodes). In contrast, as Π_h^{-1} is increased (e.g., from case 6 to case 18, from case 7 to case 16, or from case 4 to case 19), the gradient profile becomes relatively more uniform, which indicates the dominance of electromagnetic pumping leading to arc shielding. For increasing both, *Re* and Π_h^{-1}, a balance between convective cooling and electromagnetic pumping causes a quasi-nonuniform gradient profile. The thickness of the 2nd and 3rd thermal gradients (the thermally reactive zones), which is not observed for low *Re* and

Π_h^{-1}, also shows similar behavior, i.e., a nonuniform profile at high *Re* and almost uniform profile at high Π_h^{-1}. The simulation results have shown that the reactive zones consistently increase in number for large values of *Re* and Π_h^{-1} (i.e. cases 10, 14, 16, 18, 19) and might indicate the relative rise in the thermal equilibrium (similar to as seen in figure 13(c)).

7. Summary and conclusions

Industrial applications such as circuit breakers and wire arc spraying involve the interaction between an electric arc and a stream of gas impinging perpendicular to it, a configuration known as the arc in crossflow. A three-dimensional time-dependent two-temperature plasma flow model is used to computationally characterize a canonical arc in crossflow. The model is validated with experimental observations reported in the literature and its results contrasted against those from LTE models, which consider a single equilibrium temperature for all species. The two-temperature model produces consistent solutions that provide additional quantification of the deviation between heavy-species and electron temperatures compared to those from LTE models. Particularly, modeling results show that thermal nonequilibrium is dominant in the plasma-gas interaction and plasma-electrode regions. The two-temperature model is subsequently used to characterize the canonical arc in crossflow as a function of the Reynolds and Enthalpy dimensionless numbers; the former provides a measure of the strength of the gas flow, whereas the inverse of the latter, a measure of the strength of the arc. The characterization revealed the behavior of arc shape, voltage drop, arc power, and degree of nonequilibrium with varying controlling parameters. The results show that the arc power and the level of nonequilibrium increase with both, the Reynolds and (inverse) Enthalpy numbers. The plasma – gas interaction region is analyzed by defining a characteristic thermal front thickness, analogous to flame fronts in combustion systems. Analysis of this plasma front shows the development of complex structures through the arc that increases with the Reynolds and (inverse) Enthalpy numbers, and suggests the onset of unstable behavior.

Acknowledgments

The authors gratefully acknowledge support from the U.S. National Science Foundation through award CBET-1552037 and the U.S. Department of Energy through award DE-SC0018230.

References

[1] M. Kelkar and J. Heberlein 2000 Physics of an arc in crossflow *J. Phys. D: Appl. Phys.* , **33**, pp 2172-82.

[2] R. Bolot, M.-P. Planche, H. Liao, and C. Coddet 2008 A three-dimensional model of the wire-arc spray process and its experimental validation *Journal of Materials Processing Technology*, **200**, pp 94-105.

[3] X. Wang, J. Heberlein, E. Pfender, and W. Gerberich 1999 Effect of nozzle configuration gas pressure and gas type on coating properties in wire arc spray *Journal of Thermal Spray Technology*, **8**, pp 565-75.

[4] D. N. Gupta, G. N. Patil, D. Srinivas, S. S. Kale, and S. B. Potnis 2010 Numerical simulation for arc-plasma dynamics during contact opening process in electrical circuit-breakers *Journal of Physics: Conference Series*, **208**, pp 012046.

[5] W. Yi, R. Mingzhe, L. Jian, and L. Jianyong 2006 Calculation of electric and magnetic fields in simplified chambers of low-voltage circuit breakers *IEEE Transactions on Magnetics*, **42**, pp 1007-10.

[6] F. Yang *et al.* 2013 Low-voltage circuit breaker arcs—simulation and measurements *Journal of Physics D: Applied Physics*, **46**, pp 273001.

[7] B. Swierczynski, J. J. Gonzalez, P. Teulet, P. Freton, and A. Gleizes 2004 Advances in low-voltage circuit breaker modelling *Journal of Physics D: Applied Physics*, **37**, pp 595-609.

[8] D. M. Benenson, A. J. Baker, and A. A. J. Cenkner 1969 Diagnostics on steady-state cross flow arcs *IEEE Transactions on Power Apparatus and Systems*, **88**, pp 513-521.

[9] D. M. Benenson and A. A. Cenkner Jr 1969 Effect of velocity and current on temperature distribution within crossflow-blown arcs *Journal of heat transfer*, **92**, pp 276-284.

[10] H. H. Maeckar and H. G. Stablein 1986 What keeps an arc standing in a cross flow *IEEE Transactions on Plasma Science*, **14**, pp 291-299.

[11] L. Lincun, X. Weidong, Z. Heling, and M. Qiang 2007 Three dimensional modelling of a DC arc in crossflow *Plasma Science and Technology*, **9**, pp 564-69.

[12] R. O. Castro and J. P. Trelles 2015 Spatial and angular finite element method for radiative transfer in participating media *Journal of Quantitative Spectroscopy and Radiative Transfer*, **157**, pp 81-105.

[13] J. P. Trelles and S. M. Modirkhazeni 2014 Variational multiscale method for nonequilibrium plasma flows *Comput. Methods Appl. Mech. Engrg.*, **282**, pp 87-131.

[14] J. P. Trelles 2013 Computational study of flow dynamics from a DC arc plasma jet *J. Phys. D: Appl. Phys.*, **46**, pp 255201.

[15] C. Taylor and P. Hood 1972 A numerical solution of the Navier Stokes equations using the finite element technique *Computers and Fluids*, **1**, pp 73-100.

[16] T. J. R. Hughes, G. R. Feijóo, L. Mazzei, and J.-B. Quincy 1998 The variational multiscale method—a paradigm for computational mechanics *Computer Methods in Applied Mechanics and Engineering*, **166**, pp 3-24.

[17] R. Zanino 1997 Advanced Finite Element Modeling of the Tokamak Plasma Edge *Journal of Computational Physics*, **138**, pp 881-906.

[18] G. E. Georghiou, R. Morrow, and A. C. Metaxas 2000 A two-dimensional finite-element flux correct tranport algorithm for the solution of gas discharge problems *Journal of Physics D: Applied Physics*, **33**, pp 2453.

[19] U. Shumlak, R. Lilly, S. Miller, N. Reddell, and E. Sousa, "High order finite element method for plasma modeling," in *19th IEEE Pulsed Power Conference (PPC)*, 2013, pp. 1-5.

[20] E. Moreau, C. Chazelas, G. Mariaux, and A. Vardelle 2006 Modeling the Restrike Mode Operation of a DC Plasma Spray Torch *Journal of Thermal Spray Technology*, **15**, pp 524-530.

[21] E. Pfender, "Heat transfer from thermal plasmas to neighboring walls or electrodes " in *Plasma Chemistry–2: Plasma Chemistry and Transport Phenomena in Thermal Plasmas*, A. T. Bell and C. Bonet, Eds.: Pergamon, 1976, pp. 199-213.

[22] J. P. Trelles, C. Chazelas, A. Vardelle, and J. V. R. Heberlein 2009 Arc Plasma Torch Modeling *Journal of Thermal Spray Technology*, journal article **18**, pp 728.

[23] H. Guo, X.-N. Zhang, J. Chen, H.-P. Li, and K. Ostrikov 2018 Non-equilibrium synergistic effects in atmospheric pressure plasmas *Scientific Reports*, **8**, pp 4783.

[24] M. S. Benilov 2008 Understanding and modelling plasma–electrode interaction in high-pressure arc discharges: a review *J. Phys. D: Appl. Phys*, **41**, pp 144001-144030.

[25] L. Niemeyer and K. Ragaller 1973 Development of Turbulence by the Interaction of Gas Flow with Plasmas *Z. Naturforsch*, **28a**, pp 1281-1289.

[26] O. Colomés, S. Badia, R. Codina, and J. Principe 2015 Assessment of variational multiscale models for the large eddy simulation of turbulent incompressible flows *Computer Methods in Applied Mechanics and Engineering*, **285**, pp 32-63.

[27] Y. Bazilevs, V. M. Calo, J. A. Cottrell, T. J. R. Hughes, A. Reali, and G. Scovazzi 2007 Variational multiscale residual-based turbulence modeling for large eddy simulation of incompressible flows *Computer Methods in Applied Mechanics and Engineering*, **197**, pp 173-201.

[28] S. ModirKhazeni and J. Trelles, "Towards a comprehensive modelling and simulation approach for turbulent non-equilibrium plasma flows," in *22nd International Symposium on Plasma Chemistry (ISPC)*, Montreal, Canada, 2015.

[29] T. K. Bose 1972 Cross-flow blowing of a two-dimensional stationary arc *AIAA Journal*, **10**, pp 80-86.

[30] T. V. Laktyushina, G. P. Lizunkov, and O. I. Yas'ko 1992 Flow Turbulence in Cylindrical Channel Electric Arc *Journal of Engineering Physics and Thermophysics*, **62**, pp 440-445.

[31] O. I. Yas'ko 1969 Correlation of the characteristics of electric arcs *Brit. J. Appl. Phys. (J.Phys. D)*, **2**, pp 733-751.

[32] O. I. Yas'ko 1990 Some Aspects of the Generalization of Electric Arc Characteristics *Pure and Appl. Chem*, **62**, pp 1817-1824.

[33] M. Shigeta 2016 Turbulence modelling of thermal plasma flows *Journal of Physics D: Applied Physics*, **49**, pp 493001.

[34] F. T. C. Yuen and Ö. L. Gülder 2009 Premixed turbulent flame front structure investigation by Rayleigh scattering in the thin reaction zone regime *Proceedings of the Combustion Institute*, **32**, pp 1747-1754.

[35] D. Wisman and B. Ganguly 2011 Flame-Front Visualization using Argon–Oxygen Plasma Discharge *IEEE Transactions on Plasma Science*, **39**, pp 2066-2067.